［溶接学会論文集　第 41 巻　第 2 号　p. 1s-5s（2023）　DOI: 10.2207/qjjws.41.1s］

Elucidation of solidification mode of Fe-Mn-Si alloy during TIG spot welding using synchrotron X-ray*

by Tomoya Nagira**, Terumi Nakamura**, Takashi Kimura**, Fumiyoshi Yoshinaka**, Takahiro Sawaguchi**, Takayuki Yamashita***, Yasuhiro Aoki*** and Hidetoshi Fujii***

High-spatial resolution synchrotron X-ray imaging was combined with X-ray diffraction for a detailed investigation of FA mode solidification in Fe-Mn-Si (FMS) alloys during tungsten inert gas (TIG) spot welding. The solidification sequence of X-ray radiographs and X-ray diffraction patterns clearly revealed that the formation of equiaxed γ-Fe dendrite occurred in front of the growing columnar δ-Fe dendrites without any observable phases in the interdendritic regions. The solidification behavior of the FMS alloy was different from the conventional FA mode for the type 304 stainless steel, in which the cellular γ-Fe was independently formed in the interdendritic regions of the primary δ-Fe. During the columnar dendrite growth of δ-Fe for the FMS alloy, the ratio of the temperature gradient to the growth velocity was remarkably decreased and solute enrichment in the remaining liquid occurred, which likely led to the formation of equiaxed γ-Fe dendrite.

Key Words: In situ observation, Solidification mode, TIG welding, Synchrotron X-ray imaging, Synchrotron X-ray diffraction

1. Introduction

The Fe-Mn-Si (FMS) alloy is a new candidate material for seismic steel dampers due to its excellent plastic fatigue life[1-2]. However, the alloy shows a high susceptibility to solidification cracking due to the austenite (A) mode solidification. Recently, this issue was overcome by changing the solidification from that in the A mode to that in the ferrite-austenite (FA) mode[3]. The solidification mode can be controlled by changing the Cr /Ni equivalent ratio.

For the FMS alloy solidifying in the FA mode, ferrite (δ-Fe) was hardly observed due to its transformation to austenite (γ-Fe) in the solid-state reaction after the primary ferrite solidification[3]. Therefore, examining the effect of γ-Fe formation on the solidification cracking susceptibility by observing the fully solidified specimen is difficult. Hence, the time-resolved and in situ observation is the most effective approach to elucidate the microstructural evolution during solidification. In recent years, several techniques for in situ observation of solidification behaviors during welding have been developed using high-speed camera[4-5], synchrotron X-ray diffraction[6-7], and synchrotron X-ray imaging[8-11].

In our previous study[11], synchrotron X-ray imaging and synchrotron X-ray diffraction were utilized to elucidate the solidification behaviors of FMS alloys during tungsten inert gas (TIG) spot welding. For the FMS alloy solidifying in the A mode, the solidification cracking easily propagated through columnar dendrite boundaries with high growth misorientation. Conversely, the FMS alloy solidifying in the FA mode showed a unique solidification behavior whereby many equiaxed γ-Fe dendrites nucleated in front of the growing columnar δ-Fe dendrites. Hence, the formation of equiaxed γ-Fe grains suppressed the propagation of the solidification cracking. However, the microstructural evolution of γ-Fe has yet be clarified due to the lack of spatial resolution.

In this study, a high-spatial resolution X-ray imaging technique was used to conduct a detailed investigation of the FA mode solidification of the FMS alloy. For comparison, the solidification behavior of type 304 austenitic stainless steel solidifying in the FA mode was also examined. The formation mechanism of equiaxed γ-Fe dendrite in the FMS alloy will be discussed in terms of the ratio of the temperature gradient to the growth velocity and solute enrichment in the liquid during solidification.

2. Experimental procedure

Fe-15Mn-11Cr-7.5Ni-4Si alloy and type 304 stainless steel solidifying in the FA mode were used. The specimens were cut into 50 × 50 mm dimensions with 200 μm thickness. The synchrotron radiation experiments were performed at the beamline 20XU of SPring-8, Japan. The X-ray energy of 28 keV was selected to obtain a sufficient contrast resolution.

Figure 1 shows the schematic of an experimental setup for in situ observation of solidification behaviors during TIG spot welding. The setup consists of an X-ray imaging detector, a flat panel sensor for X-ray diffraction, TIG welding apparatus, a specimen cell, a high-speed camera for temperature

* Received: 2022.12.26, Presented at Visual-JW2022
** National Institute for Materials Science
*** Joining and Welding Research Institute, Osaka University

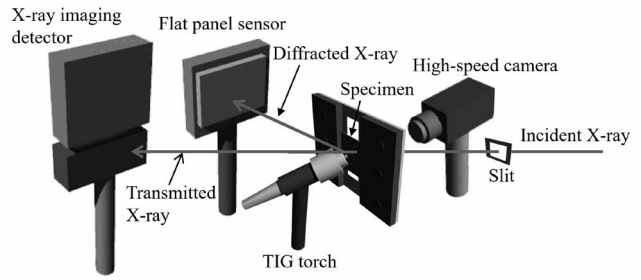

Fig. 1 Schematic of experimental setup for in situ observation of solidification behaviors during TIG spot welding using synchrotron X-ray.

measurements and a slit to limit the X-ray irradiation range. An X-ray imaging detector was used to acquire the transmitted X-ray images at 50 fps. The observation area was 1 × 1 mm, with a pixel size of 0.49 μm, which presented a higher spatial resolution than the previous study(1.1 μm/pixel)[11]. The exposure time was 20 ms. In situ X-ray diffraction (XRD) was performed simultaneously with in situ X-ray imaging of the solidification behaviors during TIG spot welding, using a flat panel sensor. A diffraction image was recorded at 60 fps with a pixel size of 200 μm. Notably, a slit was used to only obtain XRD image within the weld pool. The high-speed camera was used to record the temperature image. The temperature profile was calculated from the camera images using a two-color method software, Thermias (NAC Image Technology Inc.).

The specimen was fixed using the Cu plate and Al backing plate with a hole through which the X-ray can pass. The TIG spot welding was performed at a welding current of 6 A with an Ar shielding gas. The flow rate of Ar gas was 8 L/min. The TIG torch remained stable during welding.

The quantitative measurement of solute elements was performed by using an electron probe micro-analyzer (EPMA) for the solidified FMS alloy specimen. The specimen was quenched using Ar gas after the in situ experiment.

3. Result and discussion

3.1 In situ observation of solidification behaviors

Figure 2(a–d) shows the solidification sequence of X-ray radiographs during TIG spot welding for the FMS alloy. The observation area was limited to the center region of the weld pool by the slit placed along the X-ray path. The black triangle at the bottom indicates the tip of the tungsten electrode for TIG welding. The sequence of XRD patterns corresponding to the X-ray radiographs of Fig. 2(a–d) are shown in Fig. 2(f–i). Figure 2(a) shows the weld pool after arc ignition. This is identified by the hallo pattern of Fig. 2(f). When the arc was extinguished, the primary columnar dendrite grew toward the center of the weld pool at 0.02 s (Fig. 2(b)). The 200 and 211 reflections of δ-Fe appeared immediately after the columnar dendrite growth, as shown in Fig. 2(g). Following this, the high-spatial resolution X-ray imaging enabled us to clearly observe the nucleation of many equiaxed dendrites in front of the growing columnar dendrites, as shown in the arrows of Fig. 2(c). The growth of the columnar dendrite of δ-Fe was prevented by the formation of equiaxed dendrites. The diameter of equiaxed dendrite envelope connecting the primary dendrite arm tips grew from approximately 80 μm at 0.04 s (Fig. 2(c)) to approximately 200 μm at 0.06 s (Fig. 2(d)). This indicates that the columnar-to-equiaxed transition occurred during solidification. During this time, the 200 and 220 reflections of γ-Fe appeared while the 200 and 211 reflections of δ-Fe remained unchanged, as shown in Fig. 2(h and i). The magnified image showing the columnar-to-equiaxed transition in Fig. 2(d) is reflected in Fig. 2(e). No other phases or inclusions were observed in the interdendritic regions of δ-Fe with the high-spatial resolution X-ray imaging. These results indicate that primary columnar δ-Fe dendrites growth occurred, followed by the nucleation of equiaxed γ-Fe dendrite in front of the growing columnar δ-Fe dendrites. After solidification, all reflections of δ-Fe disappeared

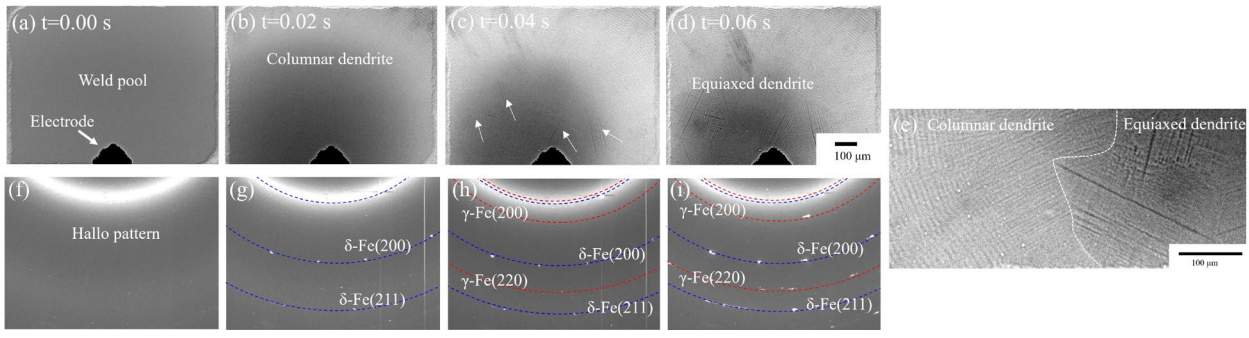

Fig. 2(a–d) Solidification sequence of X-ray radiographs during TIG spot welding for the FMS alloy, where the arrows show the equiaxed dendrites (e) Magnified image in (d) showing the columnar-to-equiaxed transition. (f–i) Sequence of XRD patterns corresponding to the X-ray radiographs of (a–d).

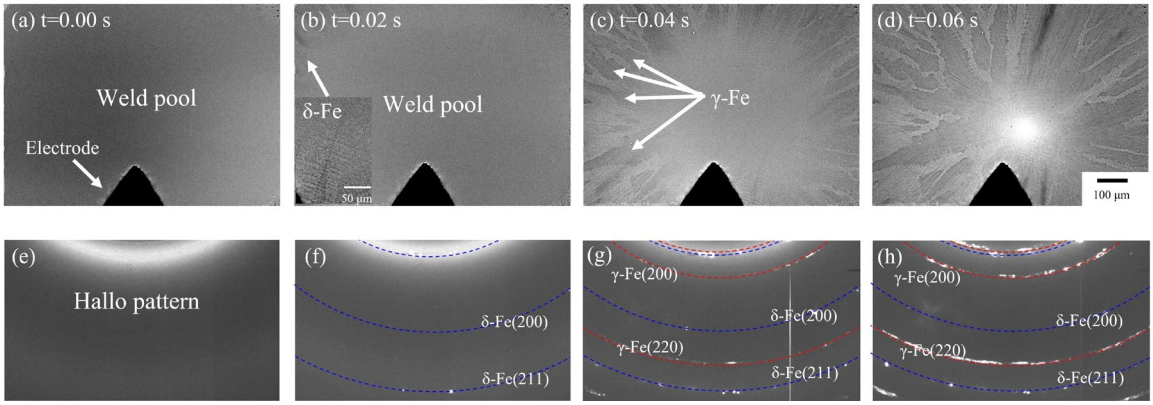

Fig. 3 (a-d) Solidification sequence of X-ray radiographs during TIG spot welding for the type 304 stainless steel. (e-h) Sequence of XRD patterns corresponding to the X-ray radiograph of (a-d).

due to the solid-state transformation from the δ phase to the γ phase.

Figure 3 (a–d) shows the solidification sequence of X-ray radiographs during TIG spot welding for the type 304 stainless steel. The sequence of XRD patterns corresponding to the X-ray radiographs of Fig. 3(a–d) is shown in Fig. 3(e–h). Figure 3(a) shows the weld pool after arc ignition, which corresponds to the hallo pattern in Fig. 3(e). After arc extinction, the formation of columnar dendrites occurred from the weld pool boundary. An expanded view of the columnar dendrite is shown in Fig. 3(b). XRD patterns in Fig. 3(f) indicated the 200 and 211 reflections of δ-Fe. Immediately after the columnar dendrite growth, the cellular dendrites with a darker contrast grew independently between the columnar dendrites. The 200 and 220 reflections of γ-Fe dendrite appeared simultaneously, as shown in Fig. 3(g). These results indicate that the columnar δ-Fe dendrite grew initially, followed by the formation of γ-Fe with a cellular microstructure in the interdendritic regions of δ-Fe. The FA mode solidification was identified by the in situ observation of solidification behavior. Although austenite is expected to be formed through the peritectic/eutectic reaction according to the phase diagram, austenite is known to be formed independently [12-13]. Inoue et al. [12] examined the solidification sequence of austenitic stainless steel solidified in the FA mode by observing the weld metal quenched by liquid Sn. The austenite in their work showed the cellular morphology in the interdendritic regions of ferrite. These results were equivalent to the in situ observation of microstructural evolution for the type 304 stainless steel. Overall, it was found that the FMS alloy solidified in different FA mode contrary to the conventional austenitic stainless steel (type 304) even under the same welding conditions.

3.2 Possible mechanism of equiaxed grain formation

The FA mode solidification for the FMS alloy was accompanied by the equiaxed grain formation of γ-Fe, as shown

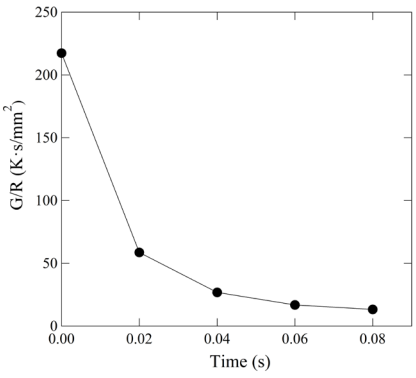

Fig. 4 Time dependence of the G/R for the FMS alloy.

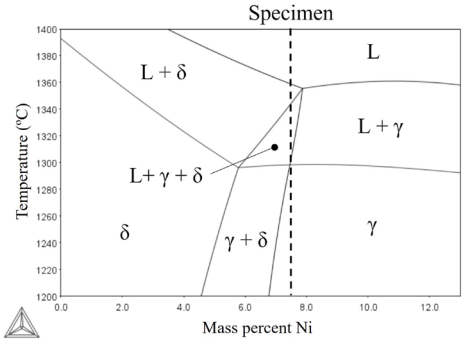

Fig. 5 Phase diagram of the Fe-Mn-Cr-Ni-Si alloy. Black dotted line shows the composition of the FMS alloy.

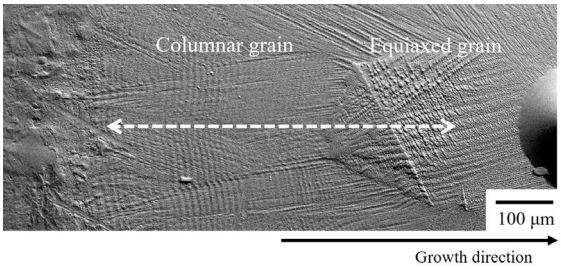

Fig. 6 FE-SEM image of the quenched specimen after the in situ experiment.

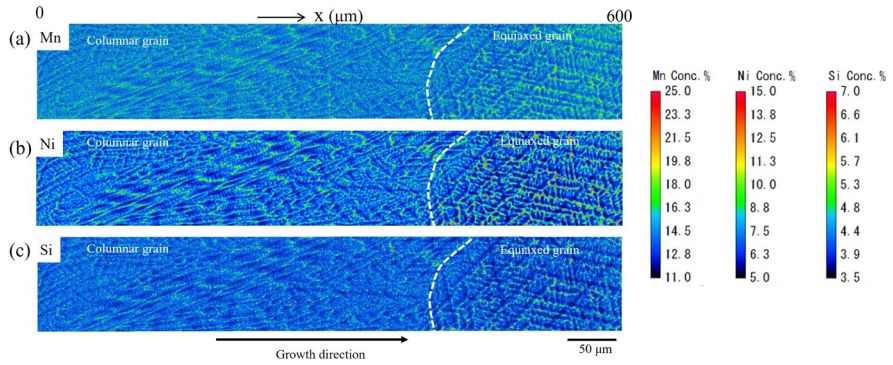

Fig. 7 EPMA mappings of (a)Mn, (b) Ni, and (c) Si for the longitudinal section of the quenched specimen. White dotted line shows the boundary between columnar and equiaxed grains.

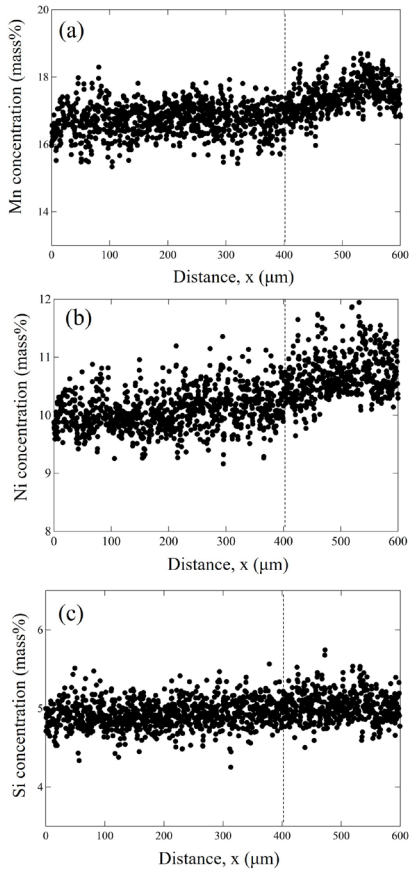

Fig. 8 Concentrations of (a)Mn, (b)Ni, and (c)Si between the dendrite arms as a function of distance. Black dotted line shows the boundary between the columnar and equiaxed grains.

in Fig. 2. The equiaxed dendrite is generally formed through heterogeneous nucleation, dendrite fragmentation, and grain detachment [14-16]. However, no nucleation site for γ-Fe was observed even with the high-resolution X-ray imaging.

The columnar-to-equiaxed transition can be analyzed in terms of the ratio of the temperature gradient(G) to the local solidification velocity (R) [14-15]. G at the solid/liquid interface was calculated from the temperature images recorded by the high-speed camera. The solid/liquid interface was determined according to the solidification sequence of X-ray radiographs. Figure 4 shows the time dependence of the G/R ratio for the FMS alloy during the columnar dendrite growth of δ-Fe. Notably, the in situ experiment was performed without using the slit to observe the solidification behaviors of the whole area in the weld pool and the growth velocity was measured by tracing the tip of the dendrite growth. As the columnar dendrite growth progressed, the G/R ratio decreased remarkably due to the increase in R and decrease in G; the ratio decreased to approximately one-tenth its original value just before the equiaxed dendrite growth occurred. Therefore, the columnar-to-equiaxed transition may be caused by the significant decrease in the G/R ratio due to the increase in the constitutional undercooling. The dependence of G/R on the columnar-to-equiaxed transition of the crystal for the FMS alloy necessitates further investigation under various welding conditions in a future study.

According to the phase diagram for the FMS alloy, calculated by the Thermo-Calc software and TCFE11 database, as shown in Fig. 5, the composition of the FMS alloy solidifying in the FA mode (dotted line in Fig. 5) was close to that in the A mode. It is likely that increase in the Ni content in the remaining liquid during the growth of columnar δ-Fe dendrite caused the change in the solidification mode from FA to A mode. To confirm this hypothesis, the distributions of solutes (Mn, Ni, and Si) that are likely to be segregated in the liquid during the solidification for the quenched specimen were examined with EPMA analysis.

Figure 6 shows the FE-SEM image of the FMS alloy quenched using Ar gas after the in situ experiment. The equiaxed grains were located in front of the columnar grains along the growth direction. Figure 7 (a–c) shows the EPMA mappings of Mn, Ni, and Si in the longitudinal section within the white dotted two-headed arrow in Fig. 6, respectively. Notably, all ferrite fully transformed into austenite during the cooling and the δ-γ solid state transformation likely influenced the solute distribution. Mn, Ni, and Si were highly segregated between the dendrite arms.

This indicates that the dendrite growth of δ-Fe caused the enrichment of Mn, Ni and Si in the liquid during solidification. Figure 8(a–c) shows the concentration of Mn, Ni and Si, respectively, between the dendrite arms as a function of distance, which corresponds to the x in Fig. 7. The concentrations of Mn, Ni, and Cr were 12.6 %, 40 %, and 22.5 % higher than the nominal composition (15Mn-7.5Ni-4Si), respectively, at the boundary between the columnar and equiaxed grains (x = 400 μm), as shown by the black dotted line in Fig. 8. This indicates that the composition of the liquid in front of the growing solid–liquid interface shifted to the composition range of the A mode solidification due to the solute enrichment, which likely caused the change of the solidification mode during solidification. Lippold et al. [17] reported that Ni enrichment in the liquid during solidification caused the shift in the solidification mode from primary ferrite to primary austenite for the weld metal of the type 310/304 stainless steel. Therefore, the nucleation of equiaxed γ-Fe dendrite for the FMS alloy is likely to occur due to the solute enrichment in the remaining liquid during solidification.

4. Conclusions

The time-resolved and in situ observation of solidification behaviors for the FMS alloy and type 304 stainless steel solidifying in the FA mode, during TIG spot welding was performed using a synchrotron X-ray imaging combined with synchrotron X-ray diffraction. The following conclusions can be drawn.

1. The equiaxed grain formation of γ-Fe in front of the growing columnar δ-Fe dendrites was clearly identified by utilizing high-spatial resolution X-ray imaging. In contrast, cellular γ-Fe was formed independently in the interdendritic regions of the primary δ-Fe for the type 304 stainless steel. The FA mode of the FMS alloy was different from the conventional FA one of the type 304 stainless steel.
2. G/R ratio was remarkably decreased during the growth of the columnar δ-Fe dendrite, which likely caused the morphological change from columnar to equiaxed dendrite.
3. EPMA analysis of the quenched specimen for the FMS alloy showed that the enrichment of Mn, Ni, and Si between the dendrite arms occurred during solidification. The solute enrichment in the remaining liquid whose composition was equivalent to the primary γ-Fe solidification likely caused the nucleation of equiaxed γ-Fe dendrite.

Acknowledgements

The experiments were performed with the approval of the Japan Synchrotron Radiation Research Institute (JASRI) (Proposal No. 2020A1150, 2021A1121, 2021B1152, and 2022A1096). This paper is based on results obtained from a project, JPNP 14004, commissioned by the NEW Energy and Industrial Technology Development Organization(NEDO). This study was partially supported by the Japan Society for the Promotion of Science KAKENHI Grant Number 20K05168.

Reference

1) T. Sawaguchi et al., Designing Fe-Mn-Si alloys with improved low-cycle fatigue lives, Scr. Mater., 99 (2015), 49-52.
2) I. Nilulin et al., Effect of strain amplitude on the low-cycle fatigue behavior of a new Fe-15Mn-10Cr-8Ni-4Si seismic damping alloy, Int. J. Fatigue 88 (2016), 132-141.
3) F. Yoshinaka et al., Develpment of feffous-bsed weldable seismic damping alloy with prolonged plastic fatigue life. Scr. Mater., 197 (2021), 113815.
4) K. Kadoi et al., The effect of welding conditions on solidificaiton cracking susceptibility of type 310S stainless steel during laser welding using an in-situ observation technique, Weld. World, 57 (2013), 383-390.
5) N. Baker et al., Investigation of solidification cracking susceptibility during laser beam welding using an in-situ observation technique, Sci. Tech. Weld. Join, 23 (2018), 234-240.
6) S.S. Babu et al., Time-resolved X-ray diffraction investigation of primary weld solidification in Fe-C-Al-Mn steel welds, Acta Mater., 50 (2002), 4763-4781.
7) H. Terasaki et al., Time-resolved in-situ analysis of phase evolution for the directional solidification of carbon steel weld metal, Met. Mater. Trans. A, 37 (2006), 1261-1266.
8) L. Aucott et al., Initiation and growth kinetics of solidification cracking during welding of stee, Sci. Rep. 7 (2017), 40255
9) T. Nagira et al., Time-resolved X-ray imaging of solidification cracking for Al-Cu alloy at the weld crater, Mater. Charact., 167 (2020), 110469.
10) T. Nagira et al., In situ observation of solidfication crack propagation for type 310S and 316L stainless steels during TIG welding using synchrotron X-ray imaging, J. Mater. Sci., 56 (2021), 10653-10663.
11) T. Nagira et al., Direct observation of solidificaiton behaviors of Fe-Mn-Si alloys during arc spot welding using synchrotron X-ray, Scr. Mater., 216 (2022), 114743.
12) H. Inoue et al., Solidification mechanism of austenitic stainless steels solidified with primary ferrite. Acta Mater., 124 (2017), 430-436.
13) T. Takalo et al., Austenitic solidification mode in austenitic stainless steel welds, Metall. Trans. A, 10a (1979), 1173-1181.
14) J. C. Villafuerte et al., Mechanisms of equiaxed grain formation in ferritic stainless steel gas tungsten arc welds, Mater. Sci. Eng., A 194 (1995), 187-191.
15) T. Koseki, Solidification and solidification structure control of weld metals, Weld. Int. 16 (2002), 347-365.
16) J.A. Spittle, Columnar to equiaxed grain transition in as solidified alloys, Int. Mater. Rev., 51 (2006), 247-269.
17) J.C. Lippold et al., Solidification of austenitic stainless steel weldments: Part 2 - The effect of alloy composition on ferrite morphology, Weld. J., 59(1980), 48s-58s.